

Magnetic control of self-propelled microjets under ultrasound image guidance

Alonso Sánchez¹, Veronika Magdanz², Oliver G. Schmidt^{2,3} and Sarthak Misra¹

Abstract—This paper demonstrates closed-loop control of self-propelled microjets using feedback extracted from B-mode ultrasound images. Previous work on control of self-propelled microrobots has mainly employed video cameras equipped with microscopic lenses in order to obtain the required feedback. Nonetheless, in medical applications such as targeted drug delivery, the use of video cameras might be unsuitable for localizing microrobots that navigate within the human body. This issue is a major obstacle for transferring medical microrobotic technologies into the clinic. On that account, the first reported methods and results on control of self-propelled microjets using ultrasound equipment are provided herein. In order to exploit the microjets' self-propulsion mechanism, their motion is directed towards a predefined target by exerting magnetic torques to steer them. Binary image analysis techniques are used to estimate the microjet's position from the ultrasound images. Two air-cored coils are used to generate the steering torques within a plane. Coil currents are calculated using the estimated position error. Results show that our system employing ultrasound images allows control of microjets at an average velocity of $156 \pm 35.1 \mu\text{m/s}$ and with an average tracking error of $250.7 \pm 164.7 \mu\text{m}$. As a reference, when microscopic image feedback is used in the setup, an average velocity and tracking error of $207 \pm 25.9 \mu\text{m/s}$ and $183.2 \pm 84.31 \mu\text{m}$, respectively, are observed.

I. INTRODUCTION

Since the last decade, research in medical microrobotic applications has significantly evolved [1]. Today, it is observed that the complexity of the scenarios being studied is approaching the one of a realistic clinical case [2], [3]. Some applications that are actively investigated include: targeted drug delivery, brachytherapy, manipulation of cells, and removal of deposits in blood vessels [1]. In all these applications, the use of micro- and/or nano-scale devices potentially allows to perform less invasive diagnostic, therapeutic and surgical interventions; due to the fact that these small-scale robots might provide new ways of accessing hard-to-reach areas within the patient's body (e.g. deeply-located tumors, metastatic and/or cardiovascular diseases). However, a non-negligible number of engineering and clinical studies are still required before the general public can safely benefit

This work was supported by funds from the Netherlands Organization for Scientific Research (NWO) Innovative Medical Devices Initiative (IMDI) - Project: USE (Ultrasound Enhancement).

¹A. Sánchez and S. Misra are with MIRA Institute for Biomedical Technology and Technical Medicine (Robotics and Mechatronics group), University of Twente, 7500 AE Enschede, The Netherlands {l.a.sanchezsecades, s.misra}@utwente.nl

²V. Magdanz and O.G. Schmidt are with the Institute for Integrative Nanosciences, IFW Dresden, 01069 Dresden, Germany {v.magdanz, o.schmidt}@ifw-dresden.de

³O.G. Schmidt is also with the Material Systems for Nanoelectronics, Chemnitz University of Technology, 09107 Chemnitz, Germany

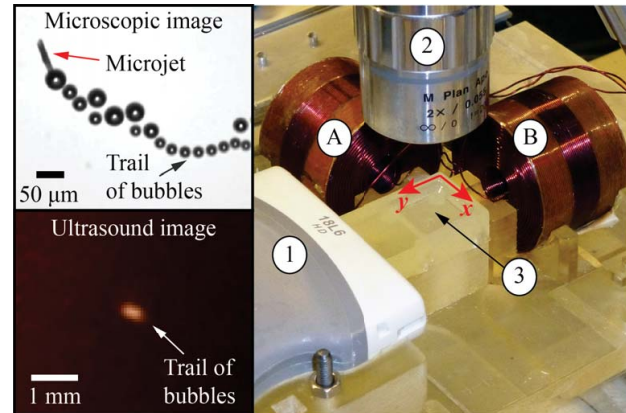


Fig. 1. Experimental setup for magnetic control of self-propelled microjets under ultrasound image guidance. Motion of microjets is controlled within a plane by actioning of coils A and B, perpendicular to each other. Magnetic torques are exerted on microjets to control their orientation, while their self-propulsion force allows them to reach a target. A Siemens ACUSON S2000 ultrasound system (Siemens Healthcare, Mountain View, USA) equipped with an 18L6HD transducer, ①, is used to acquire ultrasound images in the x - y plane. An optical microscopy system, ②, acquires images in the same plane and is used for validation. A reservoir for the microjets, ③, was manufactured using an emulsion of polyvinyl chloride (PVC) in order to obtain a satisfactory ultrasound image quality. The electromagnetic system generated a maximum field magnitude of $720 \pm 45 \mu\text{T}$.

from these medical innovations [4]. Some of the obstacles that need to be surmounted to be able to tackle a fully realistic human patient case include: (1) ensuring that a bio-compatible mechanism providing enough propulsion and/or resistance against time-varying flow rates is available [4], [5], (2) guaranteeing that the control system ensures patient safety, and (3) that a suitable real-time imaging modality to supervise and control the microrobots is available [2], [6]. This work mainly deals with the latter issue, i.e. the lack of servoing systems for micro- and/or nano-robots that include a clinically compatible imaging solution.

Among the wide set of medical imaging techniques that could be employed to localize microrobots (e.g. magnetic resonance (MR) [6], computed tomography (CT) and optical coherence tomography (OCT)); clinical ultrasound stands out as a promising alternative due to the maturity of the technology, its relatively low-cost, the possible imaging depths (~ 10 cm within the human body) and the resolution (sub-millimetric accuracy) that are found in today's commercial ultrasound systems. For these reasons, the use of ultrasound for visual servoing of magnetic microrobots is studied herein.

Related work on the use of ultrasound equipment to localize nano-scale contrast agents (CAs), i.e. superparamagnetic iron oxide nanoparticles (SPIOs), can be found in the literature [7], [8]. SPIOs have been originally used as MR CAs. However, since they are magnetic, they could also serve as robotic agents whether an adequate magnetic control system is available. Despite this fact, current studies mainly focus on the common use of SPIOs as non-robotic CAs, which are intended to facilitate the identification of a certain structure (e.g. cancerous cells) within a region-of-interest (ROI). In this context, it is often assumed that the nanoparticle-laden ROI is nearly constant-in-time during the image acquisition process. For the purposes of this work, on the other hand, a time-varying scenario with microrobots that rapidly move within the ROI and require high localization accuracy (for control) is investigated.

Results on closed-loop position control of paramagnetic microparticles under ultrasound guidance have also been previously reported [9]. Nonetheless, a significantly more challenging type of microrobotic agent is investigated herein, i.e. self-propelled microjets (hereafter referred to as jets) [10], [11]. Pictures of a jet and of the hardware setup are shown in Fig. 1. On average, jets present smaller dimensions than the microparticles employed in [9] (i.e. the former consisting of micro-tubes of about $50 \mu\text{m L} \times 5 \mu\text{m}$ dia., while the latter are micro-spheres of about $100 \mu\text{m}$ dia.). But more importantly, jets also differ from several other microrobots in that they have a powerful self-propulsion mechanism. For instance, they are known to be among the smallest and fastest self-propelled microrobots, reaching speeds up to 200 body lengths per second [5]. It has also been demonstrated that their open-loop self-propulsion is high enough to move against linear flow streams with rates over $100 \mu\text{m/s}$ [13]; and that at lower flow rates they can transport large amounts of microparticles and/or cells to a desired location [14], [15].

More generally, self-propelled magnetic microrobots, such as jets and magnetotactic bacteria [16], generate their propelling force by transforming chemical energy (available in the environment or stored in the organic or inert robot itself) into kinetic energy. Due to the presence of a magnetic material in their composition, these microrobots can also be attracted and steered using an externally generated magnetic field. In this way, their self-propulsion can be exploited to reach predefined targets. In the specific case of jets, propulsion is due to the continuous ejection of oxygen bubbles originated from a catalytic reaction on their inner platinum surface (as it will be further detailed in Section II). This mechanism imposes additional constraints to our vision system, with respect to previous work [9]. For example, having to accurately determine the position of the constantly moving jets within the trails of bubbles, and also to robustly handle occlusions due to other jets and/or objects in the ROI. Consequently, jets not only offer many interesting capabilities to be exploited in practical applications, but they also are an interesting test subject for developing and testing our ultrasound-based tracking system, due to the

forementioned precision, speed and robustness challenges.

The present work is the first study reporting the use of ultrasound to track and control self-propelled, fast-moving microrobots. Even though further research will be certainly required in order to fully exploit the whole set of capabilities that the equipment can offer (Doppler ultrasound, adaptive beamforming, raw ultrasound data processing, etc.) and to improve system performance, the feasibility of the proposed approach is demonstrated next. At the present stage, a position control system for jets, capable of submillimetric accuracy when using ultrasound images, is introduced.

The remaining sections of the paper are organized as follows: a description of the systems, the ultrasound-based visual tracking algorithm and the control strategy is given in Section II. Preliminary results are presented and discussed in Section III. And lastly, concluding remarks and future directions for research are given in section IV.

II. ULTRASOUND-GUIDED CONTROL OF MICROJETS

In this section the modeling of jets and the practical issues that were encountered in order to control them using ultrasound images are described first. The visual tracking algorithm and the control scheme that were designed and tested are also presented.

Jets consist of titanium, iron and platinum nanomembranes that are rolled-up into micro-tubes [10], [11]. In the presence of hydrogen peroxide (H_2O_2), at concentrations ranging from 5 to 15%, propulsion is achieved due to the catalysis of H_2O_2 by the platinum layer (resulting in the ejection of oxygen microbubbles from one of its ends [11]). Since the constituting nanomembranes are magnetic, forces and torques can also be exerted if an external magnetic field is applied.

The more general set of forces and torques acting on jets can be approximated through the following equations [17]:

$$\mathbf{f}_m + \mathbf{f}_p + \mathbf{f}_d = \mathbf{0}, \quad (1)$$

$$\boldsymbol{\tau}_m + \boldsymbol{\tau}_p + \boldsymbol{\tau}_d = \mathbf{0}, \quad (2)$$

$$\mathbf{f}_m(\mathbf{p}) = (\mathbf{m} \cdot \nabla)\mathbf{B}(\mathbf{p}), \quad (3)$$

$$\boldsymbol{\tau}_m(\mathbf{p}) = \mathbf{m} \times \mathbf{B}(\mathbf{p}) \quad (4)$$

where \mathbf{f}_m and $\boldsymbol{\tau}_m$ are the magnetic forces and torques along the three Cartesian directions, \mathbf{f}_p and $\boldsymbol{\tau}_p$ are the Cartesian forces and torques generated by the ejected bubbles, \mathbf{f}_d and $\boldsymbol{\tau}_d$ denote any other disturbance forces/torques acting on the jet (e.g. drag and other environmental forces), \mathbf{p} are the generalized coordinates of the jet, \mathbf{m} is the magnetic dipole moment of the jet, \mathbf{B} is the induced magnetic field, and ∇ is the gradient operator.

Information on the magnetic dipole moment (\mathbf{m}) of jets and on the identification procedure used to determine its numerical value can be found in [16]. The reported average magnetic dipole moment of a jet is $1.4 \times 10^{-13} \text{ A}\cdot\text{m}^2$ at 2 mT, with an associated cut-off frequency of 25 rad/s.

As it has been previously shown [18], a magnetic force-current map can be used to relate the magnetic forces of

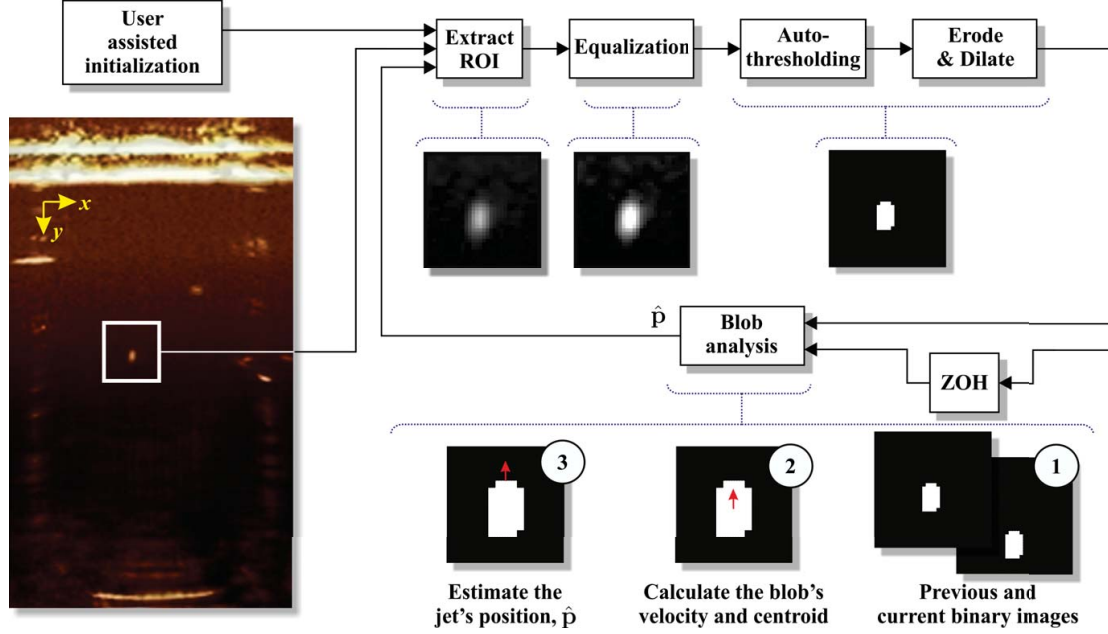


Fig. 2. The sequence of operations carried out by the visual tracking system. A region-of-interest (ROI) is initialized by the user who clicks on the computer screen with the mouse. After initialization, new ROIs are automatically defined based on the last estimated jet coordinates. Binary images are extracted every cycle from the original B-mode ultrasound image. The equalization block, adjusts the grayscale values in the ROI such that 1% of data is saturated at low and high intensities of the original ROI image. Auto-thresholding is also performed [19]. An erode/dilate operation is used to filter noise which could be present after binarization. A zero-order hold (ZOH) allows preserving the image of the previous cycle. Both, previous and current images are available at the blob analysis block in order to estimate the velocity of the jet. This tracking algorithm mainly differs from previous work with paramagnetic microparticles [9], in which the position of the jet has to be corrected by setting it at the border of the blob. To that end, an intersection point is calculated by exploring the blob image, starting at its centroid, and going along the direction of the velocity vector.

eq. (3) and the coil currents:

$$\mathbf{f}_m = \mathbf{\Lambda}(\mathbf{m}, \mathbf{p})\mathbf{I} \quad (5)$$

where $\mathbf{\Lambda}(\mathbf{m}, \mathbf{p}) \in \mathbb{R}^{m \times n}$ is the actuation matrix [18], $\mathbf{I} \in \mathbb{R}^{n \times 1}$ is the vector of applied currents, $n = 2$ is the number of electromagnetic degrees-of-freedom (DoFs) and $m = 2$ is the number of Cartesian components (see Fig. 1).

In order to calculate the required coil currents during each control cycle, an inverse solution to eq. (5) can be found by employing the Moore–Penrose pseudoinverse [18]. Moreover, a second expression relating the magnetic torque (τ_m) of eq. (4) and the coil currents (\mathbf{I}) could also be derived. Nonetheless, such magnetic torque-current map would analogously require that measurements of the jet’s angular motion are available (i.e. its orientation rather than its position) in order to perform closed-loop control. In practice, however, the orientation of a jet might not be precisely estimated from the B-mode ultrasound images and, thus, the possibility of employing the latter torque-current mapping is limited. To better understand the issue, the current implementation of the visual tracking algorithm is described next.

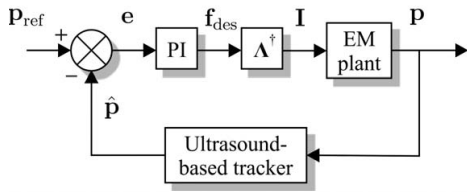
A. Ultrasound-based tracking of jets

The sequence of operations that were performed on the B-mode ultrasound images to estimate the position of a jet are illustrated in Fig. 2. The upper set of operations allow obtaining a binary image. As it can be observed from the

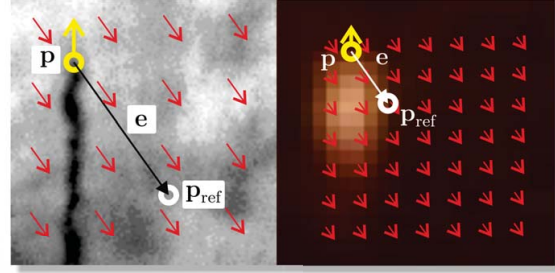
extracted ROI, the small tubular body of the jet cannot be distinguished with certainty. This observation is confirmed and further discussed in section III, through a more detailed time-sequence of images. On the other hand, the trail of microbubbles left by the jet is clearly visible. The segmented blob corresponds to this trail of bubbles. With respect to [9], in which the larger paramagnetic microparticles could be directly observed in the image, additional operations are required to calculate the position of the jet. Instead of setting the latter position at the centroid of the blob [9], the jet’s location is corrected and set to be at the border of the blob. To that end, the blob’s velocity vector is estimated from the previous and current images, and referred to the position of the blob’s centroid. Lastly, an intersection point at the border of the blob (approximately corresponding to the jet’s position) is found by exploring the blob image along the direction of the estimated velocity vector.

B. Control scheme using B-mode ultrasound image feedback

The control scheme that was employed to perform closed-loop position control of self-propelled jets is depicted in Fig. 3. In this scheme, a magnetic force (\mathbf{f}_{des}) is defined along the error vector (\mathbf{e}) pointing towards the desired position (\mathbf{p}_{ref}). A proportional-integral (PI) controller is used to guarantee that the orientation of the jets will tend to align with the magnetic field lines. On that account, the field magnitude will increase (hence the magnetic torque)



a) Control-scheme



b) Graphical representation of the control strategy

Fig. 3. Magnetic-based control scheme used to demonstrate the feasibility of closed-loop control of self-propelled microjets under ultrasound image guidance: \mathbf{p} , $\hat{\mathbf{p}}$ and \mathbf{p}_{ref} respectively are the current, estimated and desired positions of the microjet, \mathbf{e} is the position error vector, \mathbf{f}_{des} is the calculated desired force, Λ^\dagger is the Moore-Penrose inverse of the electromagnetic (EM) system's actuation matrix [18], and \mathbf{I} are the associated coil currents. Magnetic field lines are illustrated with red arrows. Yellow circles and arrows illustrate, respectively, the instantaneous position and velocity of the jet. The EM plant comprises the coils, the microjets and the environment. A proportional-integral controller (PI), with gains $K_p = 10$ and $K_i = 0.1$, is used to guarantee that the orientation of the microjets will tend to align with the magnetic field lines.

accordingly to the integral correction term, whether $\mathbf{e} \approx \mathbf{0}$.

Nevertheless, the selected control strategy implies a performance compromise, due to the fact that the instantaneous orientation of the jet could not be accurately estimated in real-time. Otherwise, a control scheme that accounts for fast perturbations (e.g. varying flow-rates deviating the jet from its desired trajectory/orientation) could be devised. As an alternative, and to be able to control the jets, it was assumed that when a weak magnetic gradient is applied, the dipole moment of the jets is such that they are not pulled by the magnetic force, but that the resulting magnetic torques will tend to align (most of the time) their main body axes along the magnetic field lines. The validity of such assumption is practically demonstrated hereafter.

III. EXPERIMENTAL RESULTS

The first results that were obtained using the proposed control strategy are presented in this section. In order to do the experiments, a current limit for each coil was set to 80 mA. This limit was experimentally determined in open-loop by linearly increasing the current up to a point where the jets inside the reservoir systematically align with the applied magnetic field, but without being attracted towards a coil. Using a Hall magnetometer (Sentro AG, Digital Teslameter 3MS1A2D3-2-2T, Switzerland) it was verified that a maximum magnetic field magnitude of $720 \pm 45 \mu\text{T}$ is applied when both coils are saturated to their maximum current value. Since our platform allows position control of jets in all directions within a plane, when using only two perpendicular electromagnets, it is experimentally verified that the jets are not being pulled by a magnetic force to operate, but that they are only steered. To more easily understand the functioning of our system and the reason why the position-based control scheme of Fig. 3 had to be chosen, a sequence of images corresponding to a jet being controlled along a linear trajectory is shown in Fig. 4. The main ultrasound imaging system parameters that were employed are summarized in Table I. In the Figure, the jet is first directed to move in one direction and then turned to

TABLE I

MAIN ULTRASOUND IMAGING SYSTEM PARAMETERS (SIEMENS ACUSON S2000, SIEMENS HEALTHCARE, MOUNTAIN VIEW, USA; EQUIPPED WITH 18L6HD TRANSDUCER). PARAMETERS ARE: ULTRASOUND FREQUENCY (FREQ.), RESOLUTION (RES.), FRAMES PER SECOND (FPS), IMAGE ACQUISITION DELAY DUE TO THE S-VIDEO CONVERSION FROM THE ACUSON S2000 VIDEO OUTPUT TO THE CONTROL COMPUTER, DYNAMIC TISSUE CONTRAST ENHANCEMENT (DTCE™) THAT PROVIDES ADVANCED SPECKLE REDUCTION AND COMBINATION WITH ENHANCED CONTRAST RESOLUTION, MAPS VALUE THAT SELECTS A PROCESSING CURVE THAT ASSIGNS ECHO AMPLITUDES TO GRAYSCALE LEVELS, AND TINT THAT APPLIES COLOR TO THE IMAGE.

Freq.	Res.	FPS	Delay	DTCE™	Maps	Tint
16 MHz	~0.1mm	25	0.5 s	High	D	5

move in the opposite one, at $t = 9\text{s}$. Once again, it can be observed from the images that the jet's body is too small to be accurately distinguished. Given the resolution of the ultrasound equipment (see Table I), it turns out that the size of a jet would correspond to less than a pixel in the ultrasound image. Therefore, the fact that the jets generate oxygen bubbles is essential for the functioning of the platform. This result also suggests that whether smaller objects, such as nanoparticles, require to be localized using ultrasound, clusters of them having a certain size need to be considered. Additionally, it might be significantly difficult to estimate the jet's instantaneous orientation from the B-mode images. If the fast jet motion and the disturbances affecting its pose are also taken into account, employing such orientation estimation for control might lead to reduced control performance and stability. For this reason, an alternative position-based control scheme was devised and tested. Lastly, it should also be observed in Fig. 4 that U-turns, and any other steep changes in orientation, should be avoided, since bubbles that are instantly coming out from the jet might be confused with those already present in its trail.

Two other types of trajectories were commanded in order

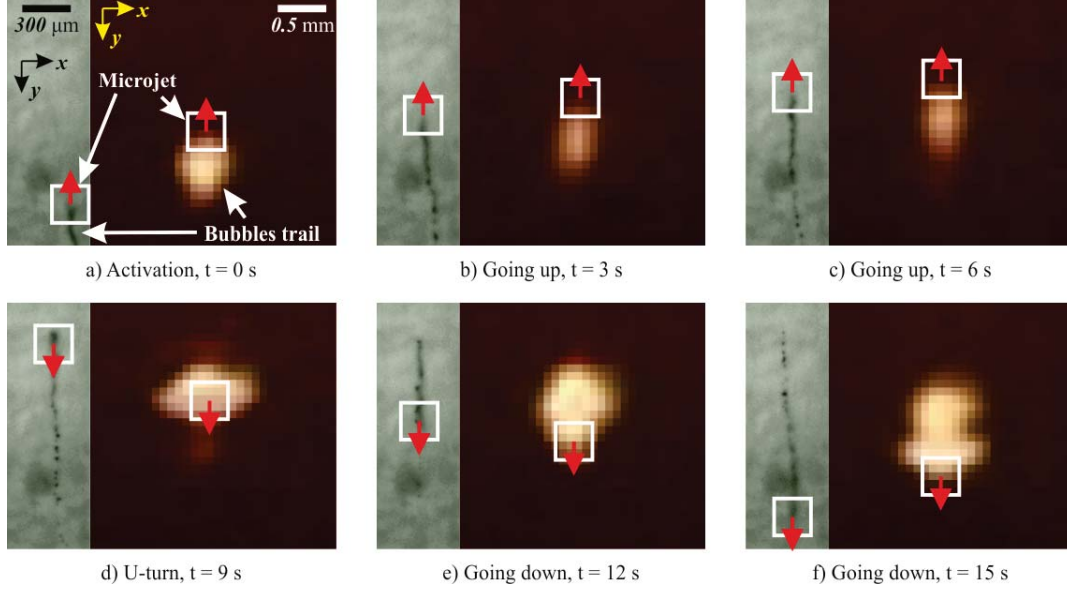


Fig. 4. Closed-loop motion control of a jet along a linear trajectory in upwards and downwards directions. At each time, microscopic and B-mode ultrasound images of the jet are respectively shown, from left to right. Red arrows in the rectangular regions-of-interest (ROIs) indicate the direction of the commanded jet's motion. An U-turn is performed at $t = 9$ s in order to invert the direction of travel. Between $t = 9$ s and $t = 12$ s bubbles being just ejected from the jet might be confused with previous ones in the trail. The trail of bubbles in the ultrasound image also appears to be larger than the one observed in the microscopic image due to the presence of: (1) image artifacts and (2) oxygen bubbles floating towards the surface of the container, which are not focused in the microscopic view, but that are still visible in the ultrasound image slice. Ultrasound slice thickness is about 0.45 mm (at the focal point) in the case of the 18L6HD transducer (Siemens Healthcare, Mountain View, USA).

to illustrate the capabilities of the system using ultrasound-based feedback:

- 1) A diamond-shaped trajectory, shown in Figure 5.a.
- 2) A figure-eight trajectory, depicted in Figure 5.b.

In both cases, the jet's average velocities and maximum tracking errors along the trajectory were calculated. Microscopic images were employed for validation, due to their higher resolution with respect to the ultrasound images. Our microscopic system included a Sony XCD-X710 (Sony Corporation, Tokyo, Japan) 1024×768 pixels FireWire camera, equipped with a Mitutoyo FS70 microscope (Mitutoyo, Kawasaki, Japan) using a M Plan Apo 2x / 0.055 objective lens. Table II, summarizes the obtained results. All values are calculated from data sequences lasting about 20 s and sampled at 25 Hz (i.e. the ultrasound image acquisition rate). Therefore, datasets of 500 samples per trial were employed. Five trials (using each time a different jet) were carried out for each trajectory, using either ultrasound-based or microscopic-based feedback. It is observed that our system employing ultrasound-based feedback allows control of microjets at an average velocity of $156 \pm 35.1 \mu\text{m/s}$ and with a maximum tracking error of $250.7 \pm 164.7 \mu\text{m}$; whereas the same system employing optical images leads to an average velocity of $207 \pm 25.9 \mu\text{m/s}$ and an error of $183.2 \pm 84.31 \mu\text{m}$. As it might be anticipated, the increased error in the system employing ultrasound is mainly due to the lower resolution of the equipment with respect to the microscopic system. Finally, these preliminary results were mainly limited by the ultrasound image acquisition rate that is currently supported

TABLE II
ABSOLUTE AVERAGE VELOCITIES AND POSITION TRACKING ERRORS.
SHOWN VALUES ARE CALCULATED OFFLINE USING THE
SIMULTANEOUSLY RECORDED MICROSCOPIC IMAGE SEQUENCES.

Feedback source	Average velocity ($\mu\text{m/s}$)	Error (μm)
Microscope	207 ± 25.9	183.2 ± 84.31
Ultrasound	156 ± 35.1	250.7 ± 164.7

by our platform (Table I) and the lack of a motorized support for the ultrasound transducer in order to always preserve the alignment between the ultrasound slice and the jet.

Please refer to the accompanying video that demonstrates closed-loop position control of a microjet under ultrasound image guidance.

IV. CONCLUSIONS AND FUTURE WORK

In this paper, motion control of self-propelled microjets using B-mode ultrasound images was demonstrated, and a platform capable of submillimetric positioning accuracy was presented. The first encountered challenges associated to the use of microjets and ultrasound images have also been addressed. To the best knowledge of the authors, these are the first reported results on the control of self-propelled microrobots using ultrasound feedback. Further developments using clinically compatible equipment for imaging and localization of medical microrobots will be crucial in

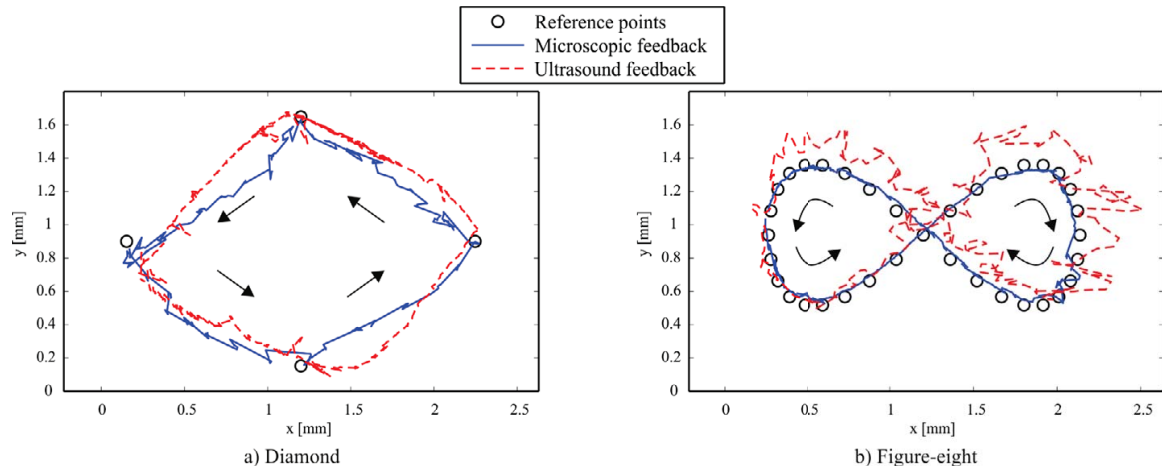


Fig. 5. Closed-loop motion control of self-propelled microjets using visual feedback extracted from B-mode ultrasound images. Jets were controlled in order to follow two different trajectories: (a) Diamond-shape and (b) Figure-eight. Desired position references are identified with black circles. The black arrows indicate the direction of the jet's motion. Performance results associated to these experiments are summarized in Table II. *Please refer to the accompanying video that demonstrates closed-loop position control of a microjet under ultrasound image guidance.*

the future, in order to guarantee their (up-to-now) expected transfer.

Additional research will be carried out in order to determine whether other ultrasound imaging functionalities (e.g. doppler imaging, raw RF-signal processing, adaptive beamforming), rather than B-mode images only, are better suited for localizing medical microrobots. Furthermore, current work is also being performed on the development of a robust visual tracking system, capable of simultaneously tracking multiple microrobots and that will also include the possibility of using ultrasound-based feedback. We also intend to modify our three-dimensional electromagnetic setup [20], in order to show the feasibility of the approach in three-dimensional space. To that end, a robotic system to position the ultrasound transducer (i.e. to keep focus of the microrobots) will be developed.

REFERENCES

- [1] Nelson, B.J., Kaliakatsos, I.K. and Abbott, J.J. Microrobots for Minimally Invasive Medicine. *Annual Review of Biomedical Engineering*, 12: 55-85, 2010.
- [2] Martel, S. Journey to the center of a tumor. *IEEE Spectrum*, 49(10): 48–53, 2012.
- [3] Bogue, R. The development of medical microrobots: a review of progress. *Industrial Robot: An International Journal*, 35(4): 294-299, 2008.
- [4] Sitti, M. Miniature devices: Voyage of the microrobots. *Nature*, 458: 1121-1122, 2009.
- [5] Sanchez, S., Ananth, A.N., Fomin, V.M., Viehrig, M. and Schmidt, O.G. Superfast Motion of Catalytic Microjet Engines at Physiological Temperature. *Journal of the American Chemical Society*, 133(38): 14860–14863, 2011.
- [6] Martel, S., Felfoul, O., Mathieu, J.B., Chanu, A., Tamaz, S., Mohammadi, M., Mankiewicz, M. and Tabatabaei, N. MRI-based Medical Nanorobotic Platform for the Control of Magnetic Nanoparticles and Flagellated Bacteria for Target Interventions in Human Capillaries. *The International Journal of Robotics Research*, 28: 1169-1182, 2009.
- [7] Mehrmohammadi, M., Shin, T.H., Qu, M., Kruizinga, P., Truby, R.L., Lee, J.H., Cheon, J. and Emelianov, S.Y. In vivo pulsed magneto-motive ultrasound imaging using high-performance magnetoactive contrast nanoagents. *Nanoscale*, 5(22):11179–11186, 2013.
- [8] Evertsson, M., Cinthio, M., Fredriksson, S., Olsson, F., Persson, H.W. and Jansson, T. Frequency- and phase-sensitive magnetomotive ultrasound imaging of superparamagnetic iron oxide nanoparticles. *IEEE Transactions on Ultrasonics, Ferroelectrics and Frequency Control*, 60(3): 481–491, 2013.
- [9] Khalil, I.S.M., Ferreira, P., Eleuterio, R., de Korte, C.L. and Misra, S. Magnetic-based closed-loop control of paramagnetic microparticles using ultrasound feedback. *Proceedings of the IEEE International Conference on Robotics and Automation (ICRA)*, In press, 2014.
- [10] Mei, Y.F., Huang, G.S., Solovev, A.A., Bermúdez Ureña, E., Moench, I., Ding, F., Reindl, T., Fu, R.K.Y., Chu, P.K. and Schmidt, O.G. *Adv. Mater.* 20: 4085, 2008.
- [11] Solovev, A.A., Mei, Y., Bermúdez Ureña, E., Huang, G. and Schmidt, O.G. Catalytic Microtubular Jet Engines Self-Propelled by Accumulated Gas Bubbles. *Small*, 5(14): 1688–1692, 2009.
- [12] Soler, L., Martínez-Cisneros, C., Swiersy, A., Sánchez, S. and Schmidt, O.G. Thermal activation of catalytic microjets in blood samples using microfluidic chips. *Lab Chip*, 13: 4299–4303, 2013.
- [13] Sanchez, S., Solovev, A.A., Harazim, S.M. and Schmidt, O.G. Microrobots Swimming in the Flowing Streams of Microfluidic Channels. *Journal of the American Chemical Society* 133(4): 701–703, 2011.
- [14] Sanchez, S., Solovev, A.A., Schulze, S., and Schmidt, O.G. Controlled manipulation of multiple cells using catalytic microrobots. *Chem. Commun.*, 47: 698-700, 2010.
- [15] Solovev, A.A., Sanchez, S., Pumera, M., Mei, Y.F., and Schmidt, O.G. Magnetic control of tubular catalytic microrobots for the transport, assembly, and delivery of micro-objects. *Adv. Funct. Mater.*, 20(15): 2430-2435, 2010.
- [16] Khalil, I.S.M. and Misra, S. Control characteristics of magnetotactic bacteria: *Magnetospirillum magnetotacticum* strain MS-1 and *M. magneticum* strain AMB-1. *IEEE Transactions on Magnetics*, 50(4): 1–11, 2014.
- [17] Khalil, I.S.M., Magdanz, V., Sanchez, S., Schmidt, O.G. and Misra, S. The control of self-propelled microjets inside a microchannel with time-varying flow rates. *IEEE Transactions on Robotics*, 30(1):49-58, 2014.
- [18] Kummer, M.P., Abbott, J.J., Kartochovil, B.E., Borer, R., Sengul, A. and Nelson, B.J. OctoMag: An electromagnetic system for 5-DOF wireless micromanipulation. *IEEE Trans. Robot.*, 26(6): 1006-1017, 2010.
- [19] Sezginm, M. and Sankur, B. Survey over image thresholding techniques and quantitative performance evaluation. *Journal of Electronic Imaging*, 13(1): 146165, 2004.
- [20] Khalil, I.S.M., Magdanz, V., Sanchez, S., Schmidt, O.G. and Misra, S. Three-dimensional closed-loop control of self-propelled microjets. *Applied Physics Letters*, 103(17): 172404-1–4, 2013.